

Geoid anomalies and dynamic topography from convection in cylindrical geometry: applications to mantle plumes on Earth and Venus

Walter S. Kiefer* and Bradford H. Hager†

Division of Geological and Planetary Sciences, California Institute of Technology, Pasadena, CA 91125, USA

Accepted 1991 June 26. Received 1991 June 23; in original form 1990 November 28

SUMMARY

A variety of evidence suggests that at least some hotspots are formed by quasi-cylindrical mantle plumes upwelling from deep in the mantle. We model such plumes in cylindrical, axisymmetric geometry with depth-dependent, Newtonian viscosity. Cylindrical and sheet-like, Cartesian upwellings have significantly different geoid and topography signatures. However, Rayleigh number–Nusselt number systematics in the two geometries are quite similar. The geoid anomaly and topographic uplift over a plume are insensitive to the viscosity of the surface layer, provided that it is at least 1000 times the interior viscosity. Increasing the Rayleigh number or including a low-viscosity asthenosphere decreases the geoid anomaly and the topographic uplift associated with an upwelling plume. Increasing the aspect ratio increases both the geoid anomaly and the topographic uplift of a plume. The Nusselt number is a weak function of the aspect ratio, with its maximum value occurring at an aspect ratio of slightly less than 1.

Key words: convection, dynamic topography, geoid anomalies, hotspots, mantle plumes.

INTRODUCTION

Ocean hotspot swells are regions of anomalously shallow bathymetry and high rates of volcanism (Crough 1983; Okal & Batiza 1987; Clague & Dalrymple 1987). The Hawaiian Island–Emperor Seamount chain is the archetypal example of such a swell. The Cape Verde Islands and the Marquesas Islands are other examples of mid-plate hotspot swells; Iceland is an example of a hotspot located at a spreading centre. Hotspot swells also occur on the continents, for example in East Africa. In total, several dozen hotspot tracks have been recognized on the Earth. Hotspot swells may also occur on other planets. Features such as Beta Regio and Atla Regio on Venus and volcanoes in the Tharsis and Elysium provinces on Mars are regions of high topography, high geoid, and shield volcanism that are believed to be hotspot-type structures (e.g., Kiefer & Hager

1989, 1991; Schubert, Bercovici & Glatzmaier 1990).

On Earth, hotspot swells are typically about 1500 km wide and are elongated in the direction of plate motion. Most oceanic hotspot swells have a peak topographic uplift, measured in areas away from volcanic shields, of about 1 km (Crough 1983), although the Cape Verde swell may be uplifted as much as 2.4 km (McNutt 1988). This peak uplift occurs near the initiation point of the swell and the uplift amplitude then decays with distance along the strike of the swell in proportion to the square-root of distance. There is a strong positive correlation between the global distribution of terrestrial hotspots and the longest wavelength components of the geoid (Crough & Jurdy 1980; Richards, Hager & Sleep 1988). At somewhat shorter wavelengths, individual hotspots also tend to be geoid highs, although the size and shape of these more localized geoid highs depends on how the long-wavelength geoid components are filtered. For example, Crough (1982) estimated a regional geoid anomaly of 8 m for the Cape Verde Rise, whereas McNutt (1988) estimated a geoid anomaly of 12 m. A similar range in geoid amplitudes has been reported for the Hawaiian Swell (Sandwell & Poehls 1980; McNutt & Shure 1986; Richards *et al.* 1988). Although geoid anomalies of this amplitude can

* Now at: Geodynamics Branch, Code 921, Goddard Space Flight Center, Greenbelt, MD 20771, USA.

† Now at: Department of Earth, Atmospheric, and Planetary Sciences, Massachusetts Institute of Technology, Cambridge, MA 02139, USA.

be interpreted in terms of compensation within the lithosphere, this does not preclude the existence of density anomalies deeper within the mantle. Kiefer *et al.* (1986), Robinson, Parsons & Daly (1987), and Ceuleneer *et al.* (1988) have shown that inclusion of a low-viscosity asthenosphere can lead to apparent compensation depths in convection models that are arbitrarily small. Richards *et al.* (1988) analysed the spectral content of the geoid anomalies associated with hotspots globally and with the Hawaiian Swell in particular and concluded that density anomalies are required at substantial depths in the mantle beneath hotspots in order to explain the observed spectral slope.

It has long been recognized that convective upwellings can deform the boundaries of the convecting layer, producing surface topography, and that the density anomalies within the convecting layer and at the deformed boundaries will produce geoid anomalies (e.g., Pekeris 1935; Morgan 1965). Two different geometries of convective upwelling have been proposed as models for hotspots. Wilson (1963) and Morgan (1972a, b) proposed that hotspot swells and their associated volcanic island chains are formed by cylindrical convective upwellings, or mantle plumes, that rise from deep within the mantle. Such upwellings can form as the result of convective instability of a thermal boundary layer within the mantle, for example at the core–mantle boundary (e.g., Yuen & Peltier 1980; Christensen 1984; Olson, Schubert & Anderson 1987). Hofmann & White (1982) favoured a plume model in which hotspot volcanism is due to recycling of oceanic crust, with old subducted slabs being reheated at depth and ascending again as thermochemical plumes. McKenzie *et al.* (1980) and Watts *et al.* (1985) suggested a different type of convective geometry, in which hotspot swells form over the upwelling limbs of elongated convective cells. A non-convective model for hotspot volcanism involves magma eruption through propagating lithospheric cracks (Turcotte & Oxburgh 1978; Sleep 1984), but the geoid spectrum expected for this model is much flatter than observed (Richards *et al.* 1988). Also, material from the uppermost mantle should be emplaced in the crack, but at some hotspots the $^3\text{He}/^4\text{He}$ ratio (Kurz *et al.* 1983; Kurz, Meyer & Sigurdsson 1985; Kaneoka, Takaoka & Upton 1986) is much higher than for typical upper mantle material (Kurz *et al.* 1982). On the other hand, high values of $^3\text{He}/^4\text{He}$ are consistent with convective upwelling from deeper in the mantle (Kellogg & Wasserburg 1990).

In the elongated convective upwelling model, adiabatic decompression should lead to partial melting and volcanism along the entire length of the upwelling. In fact, the Hawaiian Swell and some other hotspot swells have well defined age versus distance progressions in their volcanic histories (Duncan & Clague 1985), with active volcanism confined to one end of the swell. This is consistent with a cylindrical, plume-like upwelling but not with an elongated upwelling. On the other hand, more complex distributions of volcanic activity, as in the Cook–Austral chain (Okal & Batiza 1987) or the Easter Island ‘hot line’ (Bonatti *et al.* 1977), could be related to elongated convective upwellings. Elongated upwellings are also inconsistent with the observed shapes of the seismic low-velocity anomalies associated with the Hawaiian Swell and with Iceland (Zhang & Tanimoto 1989; Tryggvason, Husebye & Stefansson 1983). In the axisymmetric plume model, elongated topographic swells

simply reflect motion of the lithosphere over the plume. Conductive cooling of the thermally elevated lithosphere should lead to square-root of age subsidence of the swell as it passes beyond the plume, in agreement with observations (Crough 1978; Detrick & Crough 1978). On the other hand, it is not obvious why such a subsidence pattern should arise if a swell were supported convectively along its entire length. Also, the sharp bends in the trends of Pacific hotspot tracks would require equally sharp bends in the geometry of convective upwellings. On Venus, the topographic swells and geoid anomalies associated with features such as Beta Regio (US Geological Survey 1984; Bills, Kiefer & Jones 1987) are consistent with approximately cylindrical upwelling plumes (Kiefer & Hager 1991).

This paper focuses on numerical modelling of the topographic uplift, geoid anomalies, and heat flow associated with mantle plumes. We show how plume geoid and topography are influenced by the model geometry and by parameters such as the Rayleigh number, the variation of viscosity with depth, and the aspect ratio. We do not consider the effects of temperature-dependent rheology in this paper. Inclusion of such effects would significantly increase the required computer time, and we believe it is preferable to thoroughly understand simpler problems before considering computationally harder problems. In a separate paper, we show that our models can successfully explain both the geoid and topography of features such as Beta Regio and Atla Regio on Venus (Kiefer & Hager 1991; Kiefer 1990).

Our models are calculated in cylindrical axisymmetric geometry, which distinguishes them from many existing studies of mantle plumes in Cartesian geometry (Parsons & Daly 1983; Detrick *et al.* 1986; Robinson *et al.* 1987; Robinson & Parsons 1988; Ceuleneer *et al.* 1988). As we show later, the choice of model geometry has a strong effect on calculations of topographic uplift and geoid anomalies. Only a few studies exist in the literature on geoid and topography for axisymmetric convection. Courtney & White (1986) calculated a limited suite of cylindrical axisymmetric models and compared their results with observations of the Cape Verde Rise. Their models were restricted to an isoviscous mantle with a conductive lid to simulate the lithosphere. Richards *et al.* (1988) examined the effects of temperature-dependent rheology on plume-generated geoid and topography. They assumed a fixed temperature field and solved only the incompressible equations of motion. Bercovici, Schubert & Zebib (1988) examined geoid and topographic uplift for spherical axisymmetric convection, but restricted their study to isoviscous convection at Rayleigh numbers less than 4×10^4 , well below the range relevant to Earth, Venus, and Mars. Although some workers have begun reporting results of 3-D numerical mantle convection models (Houseman, 1988, 1990; Glatzmaier 1988; Baumgardner 1988; Bercovici, Schubert & Glatzmaier 1989a, b; Schubert *et al.* 1990; Travis, Weinstein & Olson 1990), we have chosen to work with 2-D models. By restricting our models to two dimensions, we are able to perform calculations at higher grid resolution than is currently possible for three dimensions. As a result, we are able to calculate well-resolved models at Rayleigh numbers that approach those believed to exist in the mantles of Earth and Venus.

NUMERICAL MODELLING PROCEDURES

Finite element calculations

We use a finite element code to solve the coupled system of differential equations that govern mantle convection. We non-dimensionalize the governing equations by scaling distance according to the cylinder depth d , temperature according to the temperature contrast ΔT across the cylinder depth, and time according to d^2/κ , where κ is the thermal diffusivity. In some models, we use a flux boundary condition rather than a temperature boundary condition at the base of the convecting layer. In this case, $\Delta T = (F + Hd)d/k$, where F is the applied basal flux, H is the volumetric heating rate, and k is the thermal conductivity. In non-dimensional form, the governing equations are the incompressible continuity equation (conservation of mass),

$$\nabla \cdot \mathbf{V} = 0, \quad (1)$$

conservation of momentum for an infinite Prandtl number fluid,

$$-\nabla P + \nabla \cdot \boldsymbol{\tau}' + RaT\hat{\mathbf{k}} = 0, \quad (2)$$

and conservation of energy,

$$\frac{\partial T}{\partial t} + \mathbf{V} \cdot \nabla T = \nabla^2 T + \mu. \quad (3)$$

In equations (1) to (3), P is the pressure, T is the temperature, t is time, and $\hat{\mathbf{k}}$ is a unit vector in the vertical direction. $\boldsymbol{\tau}'$ is the deviatoric stress tensor:

$$\tau'_{rr} = 2\eta \frac{\partial V_r}{\partial r}, \quad (4a)$$

$$\tau'_{zz} = 2\eta \frac{\partial V_z}{\partial z}, \quad (4b)$$

$$\tau'_{\phi\phi} = 2\eta \frac{V_r}{r}, \quad (4c)$$

$$\tau'_{rz} = \eta \left(\frac{\partial V_r}{\partial z} + \frac{\partial V_z}{\partial r} \right). \quad (4d)$$

For axisymmetry, $\tau'_{r\phi} = \tau'_{z\phi} = 0$. V_r and V_z are the radial and vertical components of the velocity field and η is the viscosity.

The solutions to equations (1) to (3) are controlled by two dimensionless parameters. One is the Rayleigh number, which for imposed ΔT is

$$Ra = \frac{\rho g \alpha \Delta T d^3}{\eta \kappa}, \quad (5a)$$

where ρ is the density, g is the gravitational acceleration, and α is the thermal expansion coefficient. In models with an applied basal flux, the flux Rayleigh number is

$$Ra_F = \frac{\rho g \alpha (F + Hd) d^4}{\eta \kappa k}. \quad (5b)$$

The second dimensionless parameter is the internal heating parameter (McKenzie, Roberts & Weiss 1974),

$$\mu = \frac{Hd}{F + Hd}. \quad (6)$$

μ governs the relative strength of basal and internal heating, with $\mu = 0$ corresponding to heating entirely from below and $\mu = 1$ to purely internal heating.

We solve the governing equations (1 to 3) using the cylindrical axisymmetric convection code of Daly & Raefsky (1985), which solves the incompressible equations of motion using a penalty function formulation (Hughes 1987, section 4.4) and bilinear shape functions. The energy equation is solved using a streamline-upwind Petrov–Galerkin formulation (Brooks & Hughes 1982), which is more accurate than either the Galerkin method or normal upwind methods for advection-dominated flows. The code steps between solutions of the energy equation and of the equation of motion. For a given temperature field, it calculates the corresponding velocity field, which is then used to update the temperature equation for the next time-step. The code uses an implicit time-stepping routine which allows us to obtain steady-state solutions efficiently (Hughes 1987). We discuss time-dependent solutions in a subsequent section. Daly & Raefsky (1985) reported a number of comparisons between their code results and laboratory convection experiments and analytic boundary layer models. These comparisons provide a good check on the accuracy of the code.

We assume zero vertical velocity and free-slip (zero shear stress) on the top and bottom of the cylinder,

$$V_z = \frac{\partial V_r}{\partial z} = 0. \quad (7a)$$

Similarly, along the axis and outer rim,

$$V_r = \frac{\partial V_z}{\partial r} = 0. \quad (7b)$$

We apply an insulating sidewall condition along the axis and outer rim of the cylinder,

$$\frac{\partial T}{\partial r} = 0. \quad (8a)$$

In models which are heated entirely from below, we assume constant temperature boundaries, $T = 0$ on top and $T = 1$ on the bottom. For models that are partially heated from within, we still apply $T = 0$ on the top and impose a flux boundary condition on the bottom,

$$\frac{\partial T}{\partial z} = \frac{F}{k}, \quad (8b)$$

where F is the specified basal heat flux and k is the thermal conductivity.

Scaling parameters

The various scaling parameters used to dimensionalize our calculations are identified in Table 1, along with the specific numerical values assumed. Comments on several of these numerical values are in order. We assume that the convective layer thickness, d , is that for whole mantle convection. For Earth, this is 2900 km, or somewhat less if part of the D'' layer is a chemically distinct region. Because Venus is about 300 km smaller in radius than Earth, its mantle is probably 100 to 150 km thinner than Earth's

Table 1. Scaling parameters.

| | | |
|------------|-------------------------------|--|
| ρ_m | Mantle Density | 3.3 gm cm ⁻³ |
| g | Gravitational Acceleration | 980 cm s ⁻² (Earth) 887 cm s ⁻² (Venus) |
| α | Thermal Expansion Coefficient | 3·10 ⁻⁵ °C ⁻¹ |
| ΔT | Vertical Temperature Contrast | 1000 °C |
| d | Depth of Convecting Layer | 2800 km |
| κ | Thermal Diffusivity | 10 ⁻² cm ² sec ⁻¹ |
| k | Thermal Conductivity | 3 W m ⁻¹ K ⁻¹ |

mantle (Basaltic Volcanism Study Project 1981, pp. 682–685). We have therefore adopted $d = 2800$ km for use in our models. The value of ΔT given in Table 1 does not represent the entire temperature change that occurs vertically through the mantle. For example, because we assume incompressible convection, it is inappropriate to include temperature differences associated with the adiabatic gradient or with phase transitions. For the purpose of modeling geoid anomalies, topographic uplift, and heat flow anomalies, the more critical parameter is the horizontal variations of temperature within the mantle. As we discuss in more detail later, our choice of ΔT leads to a temperature contrast between the plume centre and the mean mantle of about 300 °C, a value which agrees with several lines of observational constraints.

Several of the parameters in Table 1, particularly ρ , α , and κ , are expected to vary with depth (Anderson 1987). In our models, these parameters are assumed to have constant values. Because the geophysical observables of interest are most sensitive to the upper part of the plume's thermal structure, we have chosen values of these parameters which are representative of upper mantle conditions. Viscosity is also expected to be a strong function of depth. As discussed in a later section, we explicitly include this in our models.

Calculation of topographic uplift and geoid anomalies

Having obtained the temperature and velocity fields for a given convection model, we calculate the topographic uplift, geoid anomaly, and heat flow for comparison with observations. We calculate topographic uplift from the total vertical normal stress,

$$\tau_{zz} = 2\eta \frac{\partial V_z}{\partial z} - P. \quad (9)$$

For each element in the top two rows of elements, we calculate an element average value of τ_{zz} which is assigned to the element centre. We convert the non-dimensional τ'_{zz} to dimensional units by multiplying by $\eta_0 \kappa / d^2$, or equivalently by $\rho g \alpha \Delta T d / Ra$. Here η_0 is the viscosity used to normalize the depth-dependent viscosity profile (see Fig. 8). We project these values to the surface nodes using a modified version of the pressure-smoothing algorithm of Hughes (1987, Section 4.4.1) and then calculate the horizontally averaged value of the vertical stress at the surface, $\bar{\tau}_{zz}$.

The surface topography, δh , is given by

$$\delta h = \frac{(\bar{\tau}_{zz} - \tau_{zz})}{\rho_s g}, \quad (10)$$

where ρ_s is the density of the surface layer. For continental hotspots, ρ_s is the same as ρ_m because both crust and mantle material are uplifted. For oceanic hotspots, $\rho_s = \rho_m - \rho_w$, where ρ_w is the density of sea water. In the results given in this paper, we have set $\rho_s = \rho_m - \rho_w$; thus, for continental hotspots it is necessary to multiply our results for topography by $(\rho_m - \rho_w) / \rho_m = 0.70$. We use a similar procedure to calculate the topography at the base of the convecting layer. It is necessary to include the effects of density anomalies due to topography at this interface in calculating geoid anomalies.

The geoid is a surface of constant gravitational potential, U , where U is given by the solution to Poisson's equation, $\nabla^2 U = -4\pi G \rho$. G is the gravitational constant. Our sign convention is chosen to give positive potentials for positive density anomalies. In cylindrical geometry, Poisson's equation is solved by expanding the lateral variations of temperature and of topography in terms of a series of Bessel functions, $J_0(k_n r)$, where k_n is a horizontal wavenumber. The external potential varies vertically as $\exp(-k_n z)$, and at the surface ($z = 0$), the potential is given by

$$\delta U = 2\pi G \sum_n \frac{J_0(k_n r)}{k_n} \left[\rho_s \delta h_s^n + (\rho_c - \rho_m) \delta h_c^n \exp(-k_n d) - \rho_m \alpha \int_0^d T^n(z) \exp(-k_n z) dz \right]. \quad (11)$$

Here, δh_s^n and δh_c^n are the n th harmonics of the surface topography and the core–mantle boundary topography, and $T^n(z)$ is the n th harmonic of the temperature field at depth z . The sum begins at $n = 1$, so that δU represents the anomalous potential. For models with 33 horizontal nodes, the Nyquist condition shows that we can resolve harmonics up to $n = 16$. Based on the shape of the potential spectrum, essentially all of the power in the spectrum occurs for $n \leq 10$. In order to determine the values of the harmonic coefficients and the depth integral in equation (11) as accurately as possible, we use the finite element shape functions to interpolate the temperature fields onto 129×129 node meshes. The integrations are then done using a mid-point rule. Interpolating the solutions onto finer grids does not significantly alter the integration results.

Although equation (11) formally includes the core density, ρ_c , in practice it is not necessary to specify a value for ρ_c . This is because, by analogy with equation (10), the density contrast and the topographic uplift are inversely related, with a constant product, namely

$$(\rho_c - \rho_m) \delta h_c^n = \frac{(\tau_{zz} - \bar{\tau}_{zz})}{g}.$$

Similarly, the value of the potential does not depend on whether or not an ocean is present.

The geoid anomaly is related to the potential by the expression $\delta N = \delta U / g$. Equation (11) shows that there are three contributions to the geoid anomaly. The first two terms are the contributions of the mass anomalies created by dynamic topography on the top and bottom surfaces of the convecting layer. The third term represents the contributions of mass anomalies due to thermal expansion of material within the convecting layer. For a convective upwelling, the first two contributions are positive and the third contribution is negative. The sign of the potential, and

hence of the geoid anomaly, depends on the relative balance of the three terms. For the models described in this paper, the topographic mass anomalies dominate, so that the geoid is positive over the upwellings.

In the work that follows, we present both geoid anomalies and topography in dimensional form, based on the scaling parameters of Table 1. In Table 2, we tabulate the peak values of the geoid and topography (along the axis of the cylinder) in non-dimensional form. Table 2 also identifies the model parameters for each calculation. The non-dimensional geoid and topography, $\delta N'$ and $\delta h'$, are related to the dimensional values, δN and δh , by

$$\delta N = \frac{G \rho_m \alpha \Delta T d^2}{g} \delta N' \quad (12a)$$

Table 2. Model parameters and results.

| Model # | Ra | L | γ | η_a | η_{um} | AR | Grid | G | T | Nu |
|---------|-----------------|---|----------|----------|-------------|------|------|--------|--------|-------|
| 1 | 10^5 | 0 | 0.0000 | 1 | 1 | 1 | 17 | 0.0708 | 0.1289 | 11.24 |
| 2 | 10^5 | 0 | 0.0000 | 1 | 1 | 1 | 33 | 0.0722 | 0.1374 | 10.62 |
| 3 | 10^5 | 0 | 0.0000 | 1 | 1 | 1 | 65 | 0.0733 | 0.1365 | 10.42 |
| 4 | 10^5 | 0 | 0.0000 | 1 | 1 | 1 | 17 | 0.0795 | 0.1449 | 11.24 |
| 5 | 10^5 | 0 | 0.0000 | 1 | 1 | 1 | 33 | 0.0757 | 0.1414 | 10.62 |
| 6 | 10^5 | 0 | 0.0000 | 1 | 1 | 1 | 65 | 0.0742 | 0.1373 | 10.42 |
| 7 | 3×10^4 | 0 | 0.0000 | 1 | 1 | 1 | 33 | 0.1000 | 0.1570 | 7.03 |
| 8 | 6×10^4 | 0 | 0.0000 | 1 | 1 | 1 | 33 | 0.0855 | 0.1485 | 8.94 |
| 9 | 3×10^5 | 0 | 0.0000 | 1 | 1 | 1 | 65 | 0.0557 | 0.1214 | 14.85 |
| 10 | 10^6 | 0 | 0.0000 | 1 | 1 | 1 | 65 | 0.0399 | 0.1038 | 21.73 |
| 11 | 10^5 | 1 | 0.0469 | 1 | 1 | 1 | 33 | 0.0762 | 0.1317 | 8.86 |
| 12 | 10^5 | 2 | 0.0469 | 1 | 1 | 1 | 33 | 0.0667 | 0.1046 | 6.28 |
| 13 | 10^5 | 3 | 0.0469 | 1 | 1 | 1 | 33 | 0.0608 | 0.0911 | 5.40 |
| 14 | 10^5 | 4 | 0.0469 | 1 | 1 | 1 | 33 | 0.0588 | 0.0873 | 5.24 |
| 15 | 10^5 | 5 | 0.0469 | 1 | 1 | 1 | 33 | 0.0578 | 0.0856 | 5.20 |
| 16 | 10^5 | 3 | 0.0234 | 1 | 1 | 1 | 33 | 0.0633 | 0.0991 | 6.09 |
| 17 | 10^5 | 3 | 0.0313 | 1 | 1 | 1 | 33 | 0.0624 | 0.0962 | 5.84 |
| 18 | 10^5 | 3 | 0.0391 | 1 | 1 | 1 | 33 | 0.0616 | 0.0935 | 5.61 |
| 19 | 10^5 | 3 | 0.0547 | 1 | 1 | 1 | 33 | 0.0600 | 0.0889 | 5.21 |
| 20 | 10^4 | 3 | 0.0469 | 1 | 1 | 1 | 33 | 0.1019 | 0.1185 | 2.99 |
| 21 | 10^5 | 3 | 0.0469 | 1 | 1 | 1 | 65 | 0.0609 | 0.0895 | 5.29 |
| 22 | 3×10^5 | 3 | 0.0469 | 1 | 1 | 1 | 65 | 0.0447 | 0.0754 | 6.66 |
| 23 | 10^6 | 3 | 0.0469 | 1 | 1 | 1 | 65 | 0.0312 | 0.0615 | 8.45 |
| 24 | 10^5 | 3 | 0.0469 | 0.1 | 0.1 | 1 | 65 | 0.0259 | 0.0627 | 6.49 |
| 25 | 3×10^5 | 3 | 0.0469 | 0.1 | 0.1 | 1 | 65 | 0.0192 | 0.0519 | 7.95 |
| 26 | 10^6 | 3 | 0.0469 | 0.1 | 0.1 | 1 | 65 | 0.0138 | 0.0417 | 9.73 |
| 27 | 10^5 | 3 | 0.0469 | 0.01 | 0.1 | 1 | 65 | 0.0057 | 0.0464 | 7.51 |
| 28 | 3×10^5 | 3 | 0.0469 | 0.01 | 0.1 | 1 | 65 | 0.0054 | 0.0377 | 9.08 |
| 29 | 10^6 | 3 | 0.0469 | 0.01 | 0.1 | 1 | 65 | 0.0047 | 0.0299 | 11.22 |
| 30 | 10^5 | 3 | 0.0469 | 1 | 1 | 0.5 | 33 | 0.0194 | 0.0430 | 5.06 |
| 31 | 10^5 | 3 | 0.0469 | 1 | 1 | 0.65 | 33 | 0.0315 | 0.0598 | 5.30 |
| 32 | 10^5 | 3 | 0.0469 | 1 | 1 | 0.8 | 33 | 0.0442 | 0.0747 | 5.41 |
| 33 | 10^5 | 3 | 0.0469 | 1 | 1 | 1.2 | 33 | 0.0765 | 0.1048 | 5.30 |
| 34 | 10^5 | 3 | 0.0469 | 1 | 1 | 1.4 | 33 | 0.0916 | 0.1166 | 5.17 |

Notes on Table 2

(1) L and γ are parameters that define the variation of viscosity with depth in the upper boundary layer. See Equation 14. Note that where $L=\gamma=0$ in Table 2, the boundary layer viscosity is independent of depth.

(2) η_a and η_{um} are the viscosities of the asthenosphere and transition zone layers, normalized relative to a lower mantle viscosity of 1.0. The asthenosphere is defined to be the region between non-dimensional depths $z=0.0469$ and $z=0.1406$. The transition zone is defined as the region between $z=0.1406$ and $z=0.2578$. See Figure 8.

(3) AR is the aspect ratio of the convection cell, defined as the distance from upwelling to downwelling divided by the cell depth.

(4) Grid indicates the number of nodes used in each direction. Models 1-3 used a grid that is uniformly space in both dimensions. The remaining models used a grid with uniform radial spacing and non-uniform vertical spacing, with high vertical resolution in the upper boundary layer and lower vertical resolution elsewhere, as described in the text.

(5) G and T are the non-dimensional geoid anomaly and topographic uplift along the axis of the plume, defined by Equations 12a and 12b.

and

$$\delta h = \left(\frac{\rho_m}{\rho_s} \right) \alpha \Delta T d \delta h'. \quad (12b)$$

Calculation of Nusselt number and heat flow anomalies

In addition to the geoid and topography of a plume, we are also interested in the heat transported by plumes. The non-dimensional heat flux is simply

$$q = V_z T - \frac{\partial T}{\partial z}. \quad (13)$$

Following Ho-Liu, Hager & Raefsky (1987), for each element, we calculate q at the 2×2 Gaussian quadrature points and average the four values to determine an average flux for the element. The volume-averaged flux, \bar{q} , is determined by integrating over all elements. For steady convection with temperature boundary conditions, \bar{q} is equal to the Nusselt number, Nu .

The surface heat flow anomaly is calculated by taking $q(r)$ along the surface and removing the average q in order to determine the anomalous heat flow. The surface heat flow anomaly is converted to dimensional form by multiplying by $k \Delta T/d$, where k is the thermal conductivity.

Grid resolution requirements

It is important to demonstrate that the numerical grids used have fine-enough spacing to resolve the non-linear physics. We have made an extensive series of resolution checks on our plume models using two different grid types. In one, the nodes are uniformly spaced in both the radial and vertical directions. In the second, nodes in the upper boundary layer are four times closer together than for a uniform grid with the same number of nodes. On a 33×33 node grid, there are eight rows of elements between non-dimensional heights 0.9375 and 1.0, with each row separated by 0.0078. The remaining 24 rows of elements are uniformly distributed vertically throughout the remainder of the cylinder, with a vertical spacing of 0.0391. The nodes are uniformly spaced at 0.03125 in the radial direction. We have also used non-uniform grids with 17×17 and 65×65 nodes. The spacing between nodes on these grids are multiples of two of the 33×33 node non-uniform grid described here.

A representative set of results are shown in Fig. 1, which examines the effect of varying grid resolution for a constant viscosity, $Ra = 10^5$ cylinder. This figure presents the geoid anomaly and topographic uplift at the centre of the upwelling and the Nusselt number calculated on grids with 17×17 , 33×33 , and 65×65 nodes. These quantities are shown as a percentage deviation from the results for the 65×65 uniform grid model. The symbols represent calculated values, which are connected with line segments to illustrate the trends in the data. The triangles and solid lines represent results for the uniform grid models. The squares and dashed lines represent results for the non-uniform grid models. For Nu (Fig. 1c), the two grid types give results that differ negligibly. Based on the behaviour of the curves in Fig. 1, the model results would change by only a small amount if carried out on grids larger than 65×65 nodes.

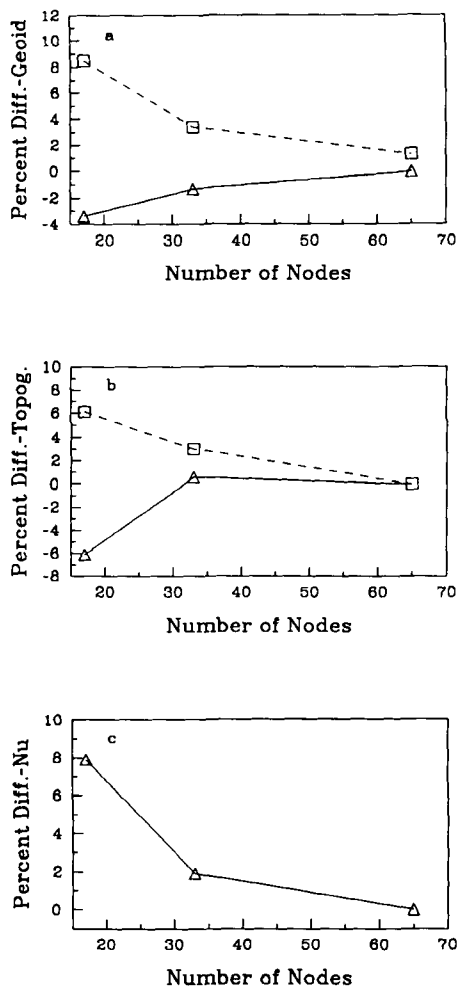


Figure 1. Convergence behaviour versus grid size for models 1–6. Triangles are calculated results for uniform grid, squares are calculated results for non-uniform grid. Results are expressed as percentage differences relative to highest resolution uniform grid case. (a) Peak geoid anomaly. (b) Peak topographic uplift. (c) Nusselt number.

Somewhat surprisingly, geoid and topography convergence as a function of grid size is more rapid on the uniform grid than on the non-uniform grid, but both grids converge to the same value. In spite of the more rapid convergence of the uniform grid, in this study we have generally made use of the non-uniform grid described above because as discussed later, the high vertical resolution (11–22 km) in the upper boundary layer of the non-uniform grid enables us to mimic the variation of viscosity with depth expected in a thermal boundary layer.

In the results that follow, our calculations are carried out on 33×33 and 65×65 grids. All models with $Ra > 10^5$ were calculated using both grids to check convergence. Models with lower Rayleigh numbers were calculated on the 33×33 grid, with a selected set of these models checked for convergence using the 65×65 grid. Based on the resolution tests in Fig. 1 and our other resolution tests, we believe that the calculations reported here are typically within ± 2 to 3 per cent of their converged values. Exceptions to this are the geoid anomalies calculated for models which include an asthenosphere (Viscosity Model 3 of Fig. 8). For these

calculations, our resolution tests suggest that our highest resolution results may be as much as 5 to 10 per cent higher than their true values at infinite grid resolution.

The other area of problematic resolution is the heat flow anomaly in models with constant viscosity. Because the thermal boundary layer is thinnest along the axis of the upwelling, resolution of the boundary layer structure is poorest there. For constant viscosity models, even our highest resolution grids do not accurately determine the heat flow anomaly near the plume axis, so we do not show heat flow anomaly results for this case. However, because the Nusselt number is defined in terms of a volume-averaged heat flux, we are able to determine Nu accurately in these models, as shown in Fig. 1(c). In most of the models described in this paper, we use a high-viscosity near-surface layer to mimic to some extent the effects of temperature-dependent viscosity. The inclusion of such a layer thickens the thermal boundary layer, so that our heat flow anomaly results are well-resolved in these cases.

BASAL VERSUS INTERNAL HEATING

In terrestrial planets, mantle convection is driven by a combination of basal heating, due to heat flowing from the core into the mantle, and internal heating, due to radioactive decay and secular cooling of the mantle. In most of the models presented in this paper, we assume an internal heating parameter of $\mu = 0$, and as noted earlier, we scale our models with a value of d appropriate for whole mantle convection. We recognize that for whole mantle convection models of the Earth, μ must be closer to 1 than to 0. Nevertheless, we believe that our models provide a reasonable model for the thermal structure of mantle plumes. There are two key questions that must be considered. Do plumes form if μ is close to unity? If plumes do form, what is the temperature contrast between a plume and the surrounding mantle? We address these issues in turn.

Do plumes form in a mostly internally heated mantle?

The value of μ is important because it determines whether or not plumes can form. As shown by Parmentier, Turcotte & Torrance (1975), if $\mu = 1$, no bottom boundary layer forms and consequently no plume can form. This is true whether or not viscosity is assumed to be temperature-dependent. However, if there is some basal heating ($\mu < 1$), then a bottom boundary layer and rising plume can form. An example is shown in Fig. 2, where we show a calculation at $\mu = 0.8$ and $Ra_F = 10^6$. A rising plume is clearly visible in this model. For comparison, Fig. 3 shows a model with $\mu = 0$.

In spherical geometry, the heat flow out of the core is concentrated into an area that is only about 25 per cent of the area of the Earth's surface. Thus, for a given μ , a model calculated in spherical geometry will have a basal heat flux per unit area which is nearly 4 times that of our cylindrical models. Thus, plumes at large μ in spherical geometry will be even more pronounced than indicated in Fig. 2. We therefore believe that our assumption of $\mu = 0$ does not significantly affect our results for the near-surface structure of plumes.

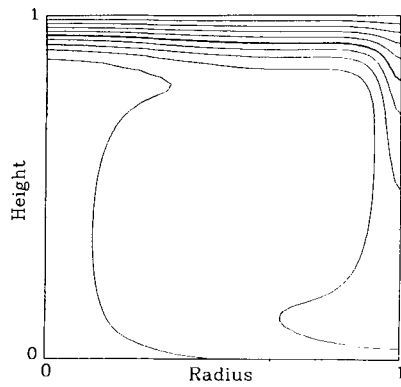


Figure 2. Temperature contours for an internally heated model at $Ra_F = 10^6$ and $\mu = 0.8$. The central axis of the cylinder is at the left, and the contour interval is 0.1 of the temperature variation in the cylinder.

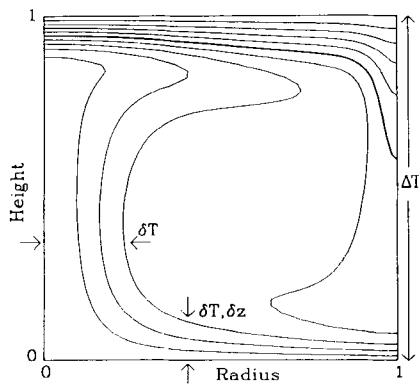


Figure 3. Isotherms for bottom-headed convection at $Ra = 10^5$ (model number 21). ΔT is the temperature contrast across the depth of the cylinder. δT is the temperature contrast across the lower thermal boundary layer and the rising plume. The contour interval is 0.1.

The temperature contrast between plumes and the surrounding mantle

The second key issue is the magnitude of the temperature contrast, δT , that exists between the plume and the surrounding mantle. (Note that δT is different from ΔT , which is the variation of temperature with depth. See Fig. 3.) The value of δT is important because the geoid anomaly, topographic uplift, and heat flow anomaly all scale linearly with the size of this temperature contrast.

For $\Delta T = 1000^\circ\text{C}$, Fig. 3 shows that δT is about 300°C . Several lines of evidence suggest that this is a reasonable estimate of the temperature contrast between plumes and normal mantle. Wyllie (1988) showed that δT of up to 300°C is consistent with the petrology of Hawaiian basalts. McKenzie & Bickle (1988) estimated that an average temperature contrast of about 200°C is necessary to produce the excess crustal thickness observed at hotspots such as Iceland; the peak contrast is presumably somewhat larger.

Richards *et al.* (1988) developed a kinematic model of the interaction between the radial outflow of material away from a plume and the flow driven by plate motions. They concluded that the stagnation line between the two flow regimes is consistent with the observed shape of the

southeastern end of the Hawaiian swell, provided that δT is around 300°C . Sleep (1990) has recently favoured a similar value. In principle, observations of heat flow anomalies can also help constrain δT . Our choice of thermal scaling predicts heat flow anomalies that are consistent with observations, although as discussed in greater detail later, our heat flow results do not tightly constrain the allowed value of δT .

For Venus, the lack of a magnetic field has been interpreted as indicating that F for Venus might be a only 50 to 80 per cent of the heat flux from Earth's core (Stevenson, Spohn & Schubert 1983). Jeanloz & Richter (1979) used a boundary layer analysis and showed that the temperature contrast across a boundary layer should be proportional to $F^{0.75}$. As Fig. 3 shows, δT is essentially the same as the vertical temperature contrast across the lower thermal boundary layer. As a result, δT for Venus should be similar to, but somewhat less than, its value on Earth. Given the uncertainties in the precise value of δT , we use the same thermal scaling for both planets.

CYLINDRICAL VERSUS CARTESIAN GEOMETRY

Figure 4 illustrates the differences between the thermal structures for Cartesian convection (Fig. 4a) and cylindrical axisymmetric convection (Fig. 4b). Both models are isoviscous, heated from below, and have $Ra = 10^5$. In the Cartesian model, the upwellings and downwellings exhibit a 180° rotation symmetry. In the cylindrical model, the

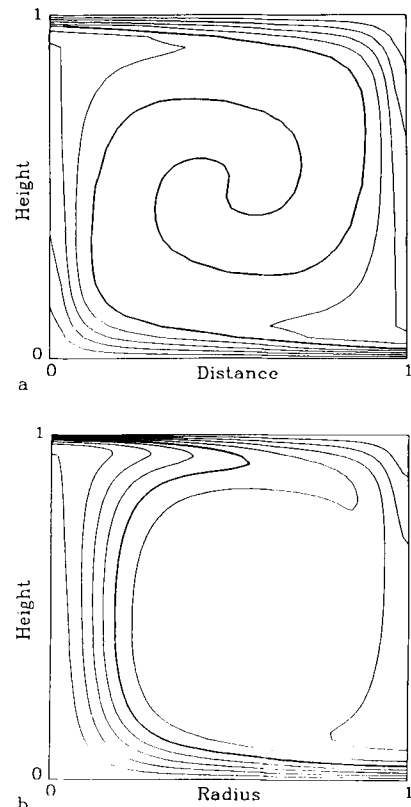


Figure 4. Isotherms for isoviscous, bottom-heated convection at $Ra = 10^5$. The contour interval is 0.1 (a) Cartesian geometry. (b) Cylindrical axisymmetric geometry (model 3).

temperature contrast across the upwelling plume is much larger than the temperature contrast across the downwelling. Because of the cylindrical geometry, the upwelling flow along the axis of the cylinder is confined to a narrow area, whereas the downwelling return flow on the outer rim occurs in a larger total area. The upwelling must therefore be more vigorous than the downwelling, producing an asymmetric thermal structure.

In Fig. 5, we compare the geoid anomalies and topography as a function of distance from the upwelling for the two thermal models of Fig. 4. The Cartesian results (dashed lines) are calculated in a manner analogous to that for the cylindrical models, except that the wavenumber expansion is in terms of $\cos(k_n x)$ rather than Bessel functions. The Cartesian results are approximately symmetric about the centre plane of the convection cell, with the lows over the downwellings having 10 to 20 per cent larger amplitudes than the highs over the upwellings. The symmetry about the mid-plane is not exact because the thermal anomalies have a rotation symmetry rather than a reflection symmetry. In contrast, the results for the cylindrical model (solid lines) are noticeably asymmetric, with the amplitudes of the highs being 2.5 to 3 times the amplitudes of the lows, reflecting the asymmetry in the underlying thermal structure. The amplitudes of the geoid and topography highs in the cylindrical case are about twice as large as in the Cartesian case, reflecting the more concentrated upwelling flow in the cylindrical case. Fig. 5 shows the importance of choosing the correct geometry when modelling the geoid and topography of mantle plumes. Given the evidence cited above for quasi-cylindrical upwellings under hotspots such as Hawaii, we believe that our models are more realistic than Cartesian geometry plume models.

Although the geoid and topography are distinctly different for cylindrical and Cartesian geometries, the heat transport

properties of the two geometries are quite similar. For isoviscous cylindrical models, we find $Nu = 10.42$ at $Ra = 10^5$ (Table 2, Model 6) and $Nu = 21.73$ at $Ra = 10^6$ (Table 2, Model 10). Blankenbach *et al.* (1989) recently published a benchmark comparison of 10 different Cartesian convection codes. They gave consensus estimates of $Nu = 10.53$ and 21.97 for the cases $Ra = 10^5$ and 10^6 in Cartesian geometry. These results differ from our cylindrical results by only about 1 per cent. Nusselt numbers for axisymmetric, isoviscous convection were previously published by Jones, Moore & Weiss (1976). They reported $Nu = 8.96$ at $Ra = 6.57 \times 10^4$, while we find $Nu = 8.94$ at $Ra = 6 \times 10^4$ (Model 8).

PARAMETRIZATION OF VISCOSITY IN THE UPPER THERMAL BOUNDARY LAYER

Because viscosity is a strong function of temperature, it varies by many orders of magnitude between the surface of a planet and the convecting interior. Although our models do not include temperature-dependent rheology, we have attempted to mimic the effect of temperature on boundary layer rheology by imposing a vertical variation of the form

$$\eta(z) = 10^{L(1-z/\gamma)}, \quad z \leq \gamma, \quad (14)$$

defining a viscosity profile normalized relative to a mantle viscosity of 1. The viscosity is 10^L at the surface ($z = 0$) and decreases exponentially with depth, reaching $\eta = 1$ at $z = \gamma$, the base of the high-viscosity zone. Our parametrization of $\eta(z)$ within the mantle ($z \geq \gamma$) is discussed in the next section. In practice, equation (14) is approximated by a sequence of 3 to 7 step function changes in η , depending on the choice of γ . For our usual choices of $L = 3$ and $\gamma = 0.0469$, six steps are used, with the viscosity changing by a factor of $\sqrt{10}$ at each step.

We investigate the effects of various values of L and γ via two sets of model calculations. In the first, illustrated in Fig. 6, we vary L and hold γ fixed at a non-dimensional value of 0.0469, corresponding to a dimensional depth of 130 km. In these calculations, the viscosity within the mantle (below the upper boundary layer) is independent of depth and the Rayleigh number is 10^5 . We vary L between 0, corresponding to a constant viscosity model, and 5, corresponding to a surface viscosity that is 10^5 times the interior viscosity.

The effects that variations in L have on the geoid anomaly, topography, and Nusselt number are shown in Figs 6(a), (b), and (c). The geoid anomaly and topography are evaluated at the plume axis. Each of the curves in Fig. 6 drops sharply as the surface viscosity increases from 1 to 10^3 and changes much more gradually with further increases in surface viscosity. The sharp drop in Nu with increasing L is easy to understand, because increasing the surface viscosity forces a thickening of the upper boundary layer and a decrease in surface velocity and leads to smaller heat flows. The decrease in geoid and topography with increasing L may seem more surprising, because a high-viscosity surface layer enhances the coupling between the convecting layer and the surface, which would lead to larger topographic uplifts and geoid anomalies. A no-slip top boundary condition would have a similar effect (Richards & Hager

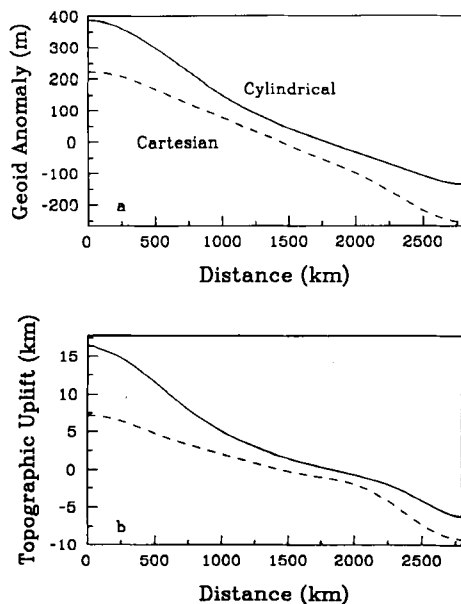


Figure 5. Profiles of geophysical observables versus distance from plume centre for cylindrical geometry (solid lines, model 3) and Cartesian geometry (dashed lines). (a) Geoid anomaly. (b) Topographic uplift.

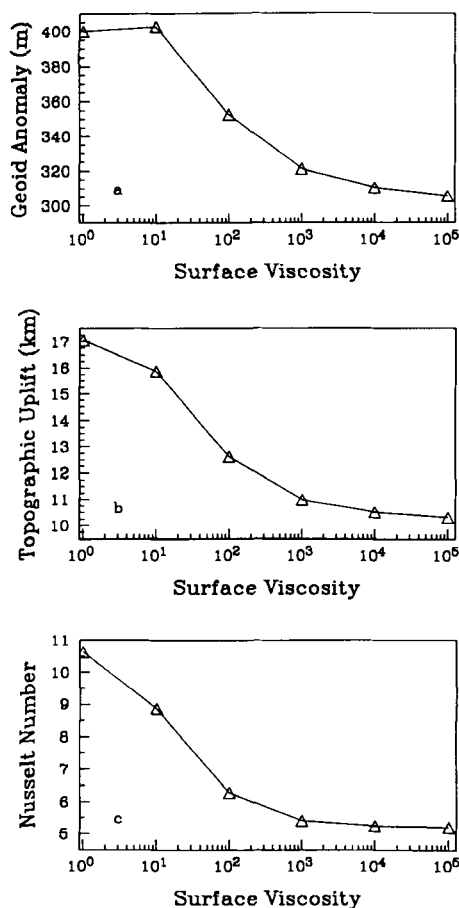


Figure 6. Effects of varying surface viscosity, shown normalized relative to the mantle viscosity. Lid thickness is 130 km ($\gamma = 0.0469$). Models 5 and 11–15. (a) Peak geoid anomaly. (b) Peak topographic uplift. (c) Nusselt number.

1984). However, this coupling effect is more than offset by changes in the thermal structure that are induced by changes in L . The horizontal variations in temperature within the mantle are much larger in isoviscous models (Fig. 4b) than in models that include a high-viscosity surface layer (Fig. 3). The larger temperature contrasts in the isoviscous case lead to the larger geoid and topography shown in Figs 6(a) and (b).

In a second series of model calculations, we hold the surface viscosity fixed using $L = 3$ and vary γ over the range 0.0234 to 0.0547, corresponding to dimensional lid thicknesses of 65 to 150 km. The effects of varying γ over this range are shown in Fig. 7, which shows how geoid anomaly, topography, and Nusselt number vary with γ . Over the range of lid thicknesses investigated, geoid and topography vary by only 5 to 10 per cent; Nu varies by 15 per cent.

In the work that follows, we adopt $L = 3$ (surface viscosity = 10^3) and $\gamma = 0.0469$ (lid thickness = 130 km) as the parameters that define the lid viscosity in our models. Although the viscosity in the boundary layer of real planets clearly varies by much more than the 3 orders of magnitude assumed here, the results of Fig. 6 suggest that results obtained using a viscosity contrast of 10^3 will not differ significantly from models with much larger viscosity

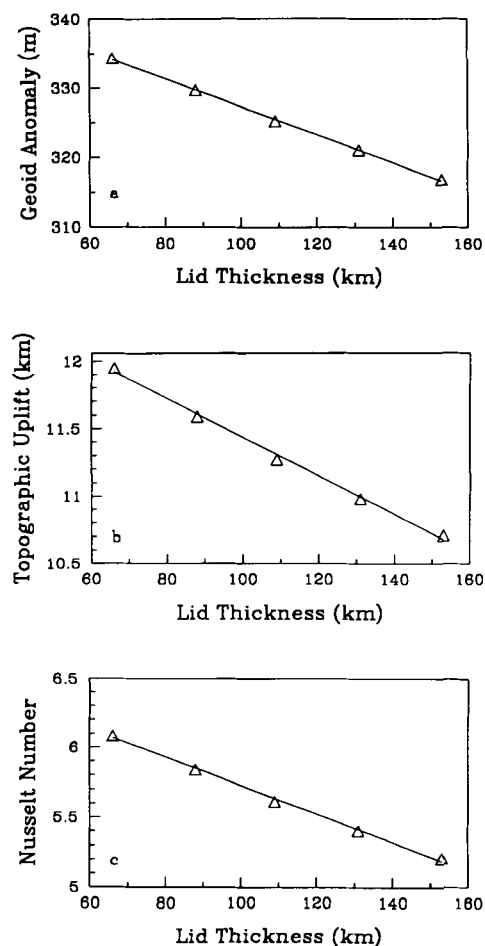


Figure 7. Effects of varying high-viscosity lid thickness. Surface viscosity = 10^3 ($L = 3$). Models 13 and 16–19. Triangles are model results, solid lines are least-squares best fit lines. (a) Peak geoid anomaly. (b) Peak topographic uplift. (c) Nusselt number.

contrasts. Our nominal lid thickness of 130 km is comparable to the lithospheric thickness in the old parts of oceanic plates. Several of the hotspots of greatest interest, such as Hawaii, Cape Verde, and Bermuda, are located on oceanic lithosphere of age 90 Myr or greater. Of course, some other hotspots, such as Iceland and the Azores, are located on spreading centres, where the lithosphere is thin. On Venus, the high surface temperature implies that the boundary layer thickness should be somewhat less than on Earth. Kaula & Phillips (1981) estimated a thermal boundary layer thickness of slightly less than 100 km for Venus. Fig. 7 shows that the difference between lid thicknesses of 100 and 130 km is slight for both the geoid and the topography. In recent years, a number of numerical models have used a conductive lid, in which both the vertical and horizontal velocity components are set to zero, as a means of simulating the thermal boundary layer structure (Courtney & White 1986; Detrick *et al.* 1986; Robinson *et al.* 1987; Ceuleneer *et al.* 1988). Our models, in which the viscosity varies continuously with depth, should be somewhat more realistic than models in which there is a discrete change between conduction and convection, but the difference between the two approaches is likely to be small.

EFFECTS OF VARIATION IN MANTLE VISCOSITY WITH DEPTH

The effects of depth variations of viscosity on convective geoid anomalies and topography have been widely recognized (Morgan 1965; Richards & Hager 1984; Ricard, Fleitout & Froidevaux 1984; Kiefer *et al.* 1986; Robinson *et al.* 1987; Richards *et al.* 1988; Robinson & Parsons 1988; Ceuleneer *et al.* 1988; Hager & Clayton 1989; Hager & Richards 1989). Within the mantles of silicate planets, the viscosity may vary continuously with depth due to the effects of pressure on rheology. The viscosity may also undergo discrete jumps at phase changes. In this paper, we consider the effects of three layers of constant viscosity. The transition depths between the layers are at non-dimensional depths of $z = 0.141$ and $z = 0.258$, corresponding to dimensional depths of 400 and 700 km. This choice of parametrization was made both because it provides a convenient way of parsimoniously parametrizing $\eta(z)$ and also because it enables a straightforward comparison with results obtained by Hager & Clayton (1989) and Hager & Richards (1989) on the depth variation of mantle viscosity on Earth. In the following discussion, we refer to the layer between 130 and 400 km as the asthenosphere, the layer between 400 and 700 km as the transition zone, and the layer below 700 km as the lower mantle.

Figure 8 shows the three standard viscosity models used in this study. The viscosity profiles are all normalized relative to the lower mantle viscosity. All three models have a high-viscosity lid defined by the parameters $\gamma = 0.0469$ and $L = 3$, as described in the previous section. Viscosity model 1 (Fig. 8a) has a high-viscosity lid and an isoviscous mantle. In viscosity model 2 (Fig. 8b), the asthenosphere and transition zone layers have a viscosity that is 0.1 times the lower mantle viscosity. In viscosity model 3 (Fig. 8c), the asthenosphere viscosity is 0.01 times that of the lower mantle and the transition zone viscosity is 0.1 times that of

the lower mantle. Model 3 is similar to the preferred Earth model of Hager & Richards (1989) and Hager & Clayton (1989), although Hager and colleagues prefer an asthenosphere viscosity that is a factor of 3 less than in model 3.

In models in which viscosity varies with depth, one must define a viscosity for determining the Rayleigh number. We use the lower mantle viscosity to parametrize Ra because the lower mantle layer always occupies at least 75 per cent of our model cylinder. Robinson *et al.* (1987) and Ceuleneer *et al.* (1988) used a similar procedure in their calculations. An alternative parametrization would be to vertically average the viscosity in some way.

Figure 9 shows profiles of geoid anomaly and topography for our three viscosity models at $Ra = 10^6$. The results for viscosity model 1 are shown in solid lines, viscosity model 2 results are in dashed lines, and viscosity model 3 results are in dot-dashed lines. These models correspond to models 23, 26, and 29 of Table 2. The presence of a low-viscosity asthenosphere reduces the efficiency with which deep convective stresses are able to couple with the surface. Thus, viscosity model 3 produces a weaker topographic uplift than is produced by the other models. As shown in Fig. 9(b), the peak topography is 7.4 km for viscosity model 1 and 3.6 km for viscosity model 3.

The geoid anomaly depends on contributions both from the mass anomalies at the uplifted surface and on thermally induced density anomalies within the convecting mantle. As Fig. 10 shows, changing the viscosity model at fixed Ra has some effect on the thermal structure. The most pronounced effect is in the region of the asthenosphere. In this region, the plume is significantly narrower than in models without a low-viscosity zone. As noted by Richards *et al.* (1988), when a hot parcel of material enters the low-viscosity zone, its velocity increases, so conservation of energy requires that

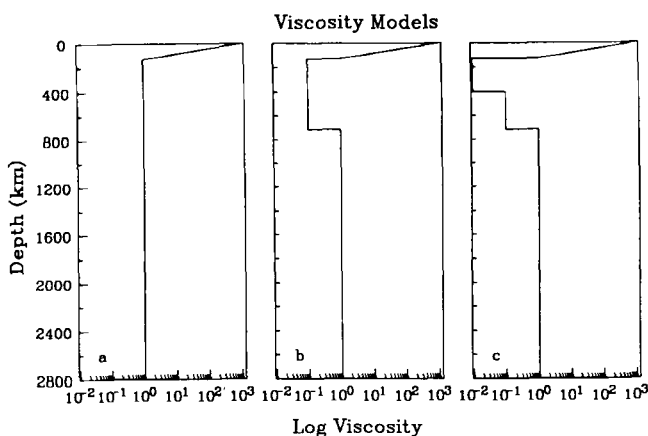


Figure 8. Viscosity versus depth profiles for the three standard viscosity models used in this study. Viscosity profiles are normalized relative to the lower mantle viscosity. All three models have high-viscosity lids defined by $L = 3$ and $\gamma = 0.0469$. (a) Viscosity model 1 has an isoviscous mantle. (b) Viscosity model 2 has an upper mantle viscosity 0.1 times the lower mantle viscosity. (c) Viscosity model 3 includes an asthenosphere with viscosity 0.01 times the lower mantle viscosity.

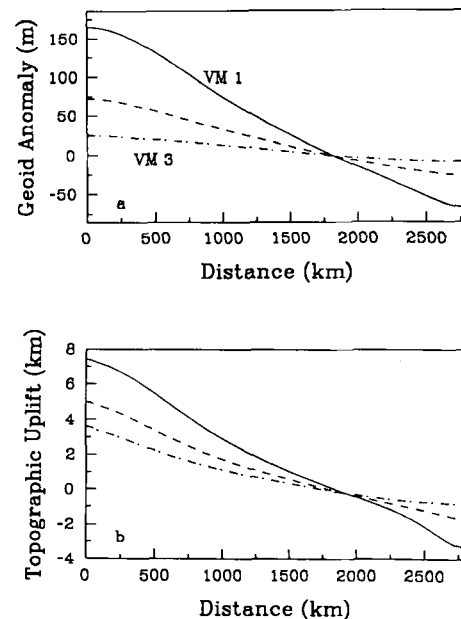


Figure 9. Profiles versus distance from plume centre for viscosity model 1 (solid lines, model 23), viscosity model 2 (dashed lines, model 26), and viscosity model 3 (dot-dashed lines, model 29). $Ra = 10^6$. (a) Geoid anomaly. (b) Topographic uplift.

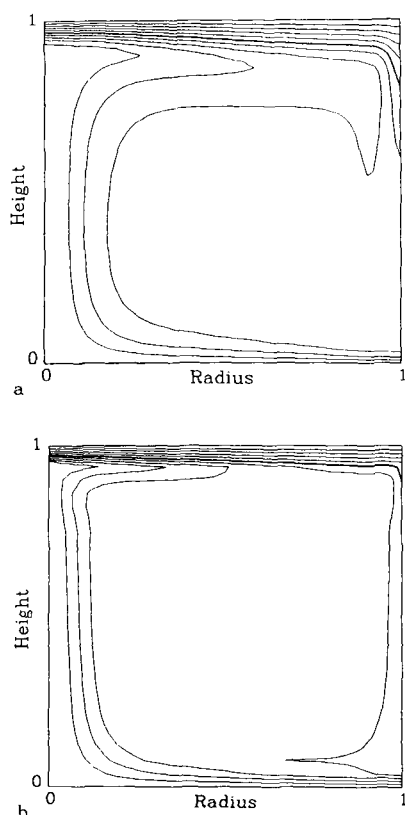


Figure 10. Isotherms as a function of viscosity model at $Ra = 10^6$. The contour interval is 0.1. (a) Viscosity model 1 (model 23). (b) Viscosity model 3 (model 29).

the plume become narrower. Also, in models with a low-viscosity zone (Fig. 10b), the near-surface outflow of material away from the plume is confined to the low-viscosity layer, whereas in models without an asthenosphere (Fig. 10a), the outflow occurs over a broader depth range. The decreased positive mass anomaly at the uplifted surface in models with an asthenosphere is more important than the decreased negative mass anomalies within the mantle, so that inclusion of a low-viscosity zone leads to significant decreases in the geoid anomaly. As shown in Fig. 9(a), the peak geoid anomaly decreases from 165 m for viscosity model 1 to only 25 m for viscosity model 3. If the asthenosphere viscosity were decreased below 0.01, the additional decrease in topographic uplift could lead to a negative geoid over the upwelling. In the Equatorial Highlands of Venus, the large amplitudes of the geoid anomalies (70 to 90 m, Bills *et al.* 1987) and topography (4 to 5 km, US Geological Survey 1984) suggest the lack of a low-viscosity asthenosphere (Kiefer & Hager 1991), a result that is consistent with earlier admittance spectrum modelling (Kiefer *et al.* 1986).

EFFECTS OF VARIATION IN RAYLEIGH NUMBER

In Figs 11 and 12, we examine how varying the Rayleigh numbers affects the geoid, topographic uplift, and heat flow associated with a mantle plume. Based on estimates of the Earth's lower mantle viscosity of 6×10^{22} to 10^{23} Poise

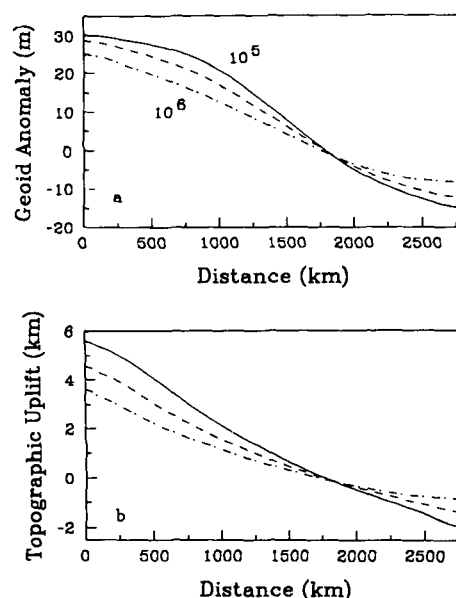


Figure 11. Profiles versus distance from plume centre for $Ra = 10^5$ (solid lines, model 27), $Ra = 3 \times 10^5$ (dashed lines, model 28), and $Ra = 10^6$ (dot-dash lines, model 29). Viscosity model 3. (a) Geoid anomaly. (b) Topographic uplift.

(Nakada & Lambeck 1989; Hager 1991) and the other parameters of Table 1, the Earth's Rayleigh number should be about $2\text{--}3 \times 10^6$. We have only calculated models up to $Ra = 10^6$, but the power-law relationships derived below can be used to estimate geoid and topography amplitudes at higher Ra .

Figure 11 shows profiles of geoid and topography for $Ra = 10^5$ (solid line), $Ra = 3 \times 10^5$ (dashed line), and $Ra = 10^6$ (dot-dashed line). The results are for viscosity model 3 (Models 27, 28, and 29 of Table 2). Both the geoid anomaly and the topographic uplift are decreasing functions of Ra . Using the scale parameters of Table 1, the peak geoid anomaly over the upwelling decreases from 30 m at $Ra = 10^5$ to 25 m at $Ra = 10^6$. As shown in Fig. 12(a), the geoid anomalies of other viscosity models are much more sensitive to variations in Ra . The peak topographic uplift over the upwelling also decreases in amplitude, from 5.6 km at $Ra = 10^5$ to 3.6 km at $Ra = 10^6$.

In dimensionalizing the calculations shown in Fig. 11, we have held the quantity $\rho g \alpha \Delta T d^3 / \kappa$ fixed, so that increasing Ra is equivalent to decreasing η . The topographic uplift then is a decreasing function of Ra . The causes of the decrease in topographic uplift with increasing Ra are readily understood. The surface topography produced by mantle convection receives contributions both from thermal anomalies in the near-surface thermal boundary layer and from thermal anomalies in the upwelling and downwelling limbs of the convection cell. With increasing Ra , the upwellings, downwellings, and thermal boundary layers all become narrower. (Compare Figs 3 and 10a.) Density anomalies within the thermal boundary layer produce topography in a manner that is essentially equivalent to Pratt compensation, so that as the boundary layer is thinned, the amount of topographic uplift that it can support is decreased. The narrowing of the upwellings and downwellings with increasing Ra implies that in the spectral

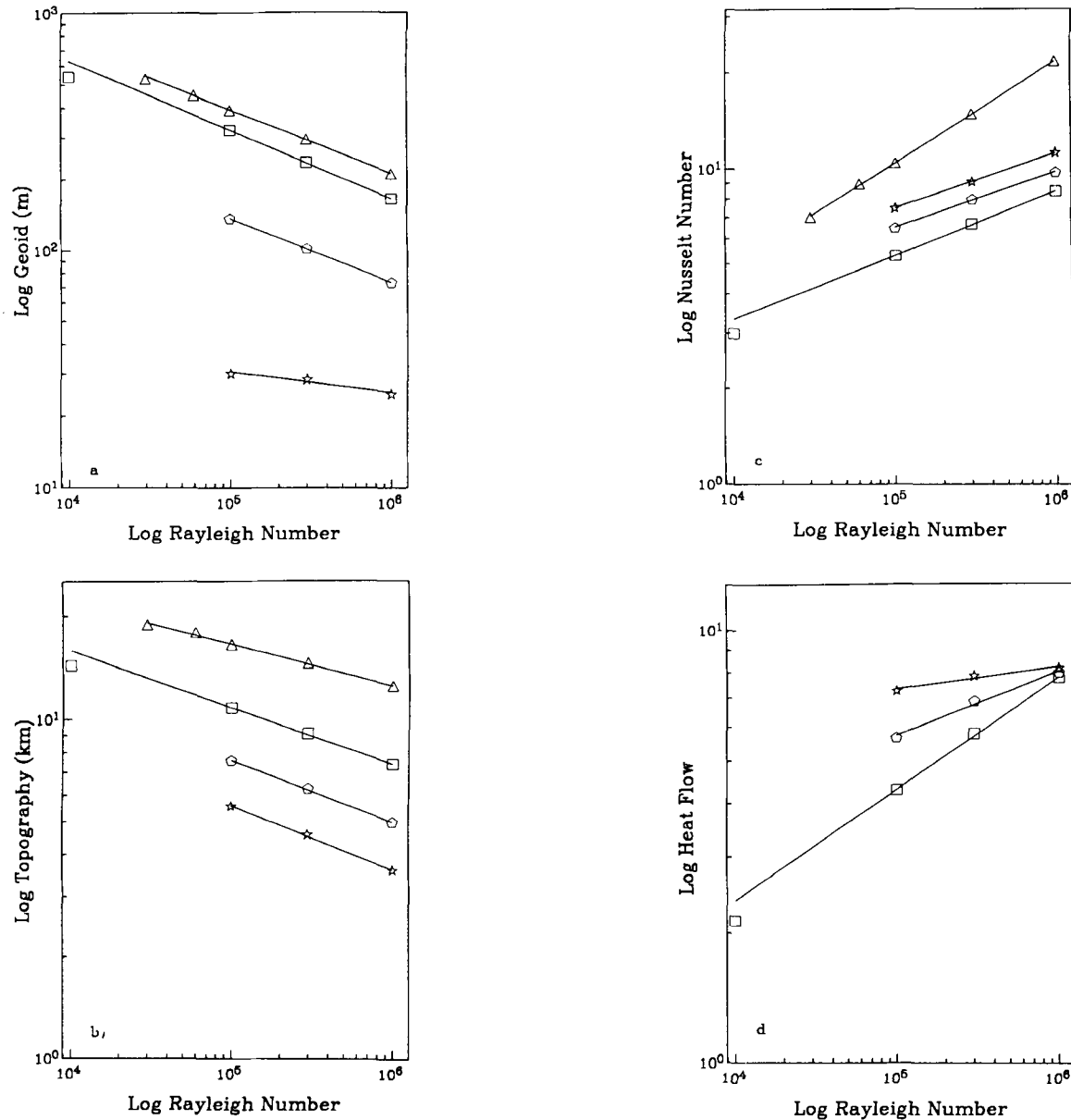


Figure 12. The lines are power-law fits to model results as discussed in the text. Triangles denote constant viscosity models (models 6–10), squares are viscosity model 1 (models 20–23), pentagons are viscosity model 2 (models 24–26), and stars are viscosity model 3 (models 27–29). (a) Log Rayleigh number versus log geoid. (b) Log Ra versus log topography. (c) Log Ra versus log Nusselt number. (d) Log Ra versus log heat flow anomaly.

domain, there is a decrease in power at long wavelengths, accompanied by an increase in power at short wavelengths. Short wavelengths do not couple as efficiently to the surface as longer wavelengths do, and hence they produce less topographic uplift. Together, these two effects produce the observed decrease in topographic uplift with increasing Ra . The decreasing topography and narrower boundary layers also imply a decreasing geoid with increasing Ra .

In contrast, Davies (1986) increased Ra by increasing ΔT , which implies that the topographic uplift increases with increasing Ra . Although controlling the value of Ra by varying the value of ΔT is a fluid dynamically acceptable choice, it produces misleading results when applied to real planets. Because viscosity is a strong function of temperature, small increases in ΔT will lead to large

decreases in η . Thus, we prefer to hold ΔT constant and vary Ra by varying η .

In Cartesian geometry, it is well known that if the Rayleigh number is high enough that well developed boundary layers form, then the Nusselt number can be written as a power-law function of Ra . A similar relationship between Ra and Nu also exists in cylindrical geometry, and relationships also exist between Ra and the geoid, the topography, and the peak heat flow. In Fig. 12, we show the relationships between Ra and the other quantities, plotted as log-log figures, so that a power-law relationship follows a straight line. The triangles are results for constant viscosity, the squares are for viscosity model 1, the pentagons for viscosity model 2, and the stars for viscosity model 3. In each case, the lines represent

Table 3. Power-law parameters.

| | Geoid | | Topography | |
|--------------------|------------------|--------|------------|--------|
| | a | b | a | b |
| Constant Viscosity | $8.7 \cdot 10^3$ | -0.269 | 66 | -0.121 |
| Viscosity Model 1 | $9.1 \cdot 10^3$ | -0.290 | 72 | -0.164 |
| Viscosity Model 2 | $3.2 \cdot 10^3$ | -0.273 | 62 | -0.182 |
| Viscosity Model 3 | $8.1 \cdot 10^1$ | -0.084 | 51 | -0.192 |

| | Nusselt Number | | Heat Flow | |
|--------------------|----------------|-------|-----------|-------|
| | a | b | a | b |
| Constant Viscosity | 0.27 | 0.319 | --- | --- |
| Viscosity Model 1 | 0.51 | 0.203 | 0.22 | 0.258 |
| Viscosity Model 2 | 0.86 | 0.176 | 1.06 | 0.147 |
| Viscosity Model 3 | 1.01 | 0.174 | 4.13 | 0.050 |

least-squares best fitting lines, calculated using only points with $Ra \geq 10^5$. For the constant viscosity model, the derived power laws also provide a good fit to model results with Ra as low as $Ra = 3 \times 10^4$. For viscosity model 1, the results for $Ra = 10^4$ begin to deviate from the power-law relationship, reflecting the absence of well-developed boundary layers at this relatively low Ra . Table 3 shows the derived power-law parameters, expressed in terms of $f(Ra) = a(Ra)^b$, where a and b are constants. The geoid, topography, and heat flow results refer to the peak values along the axis of the upwelling, dimensionalized (Table 1) in units of metres (geoid), kilometres (topographic uplift), and mW m^{-2} (heat flow).

Figure 12(a) shows that the geoid anomalies for viscosity model 3 are a much weaker function of Ra than is observed for the other viscosity models. We find a power-law exponent of only $b = -0.084$ for viscosity model 3, whereas the other viscosity models have exponents in the range -0.27 to -0.29 . There is also some suggestion of curvature in the Ra -geoid relationship for viscosity model 3, but we cannot fully define this on the basis of only 3 model points. In the Cartesian geometry results of Robinson & Parsons (1988, Fig. 10), the geoid anomaly also appears to be a weaker function of Ra in models with a low-viscosity layer than in models without a low-viscosity layer. However, this flattening of the Ra -geoid relationship does not appear to be as strong in their work as it is in our results. A quantitative comparison cannot be made because they did not tabulate power-law parameters for their results.

We noted earlier that for our constant viscosity models, our values for Nu agree closely with those observed in Cartesian geometry. Consequently, the power-law parameters for the two geometries are also quite similar. For example, Ho-Liu *et al.* (1987) gave $b = 0.326$ for the isoviscous Cartesian case. Using the same volume averaging technique, we find $b = 0.319$ for our isoviscous cylindrical models.

Although all of the models reported in this paper use a free-slip top boundary, the models with a high-viscosity lid have very low flow velocities at the top surface and behave as if the top surface were nearly rigid. In Cartesian geometry, both analytic and numerical studies of convection

with rigid boundaries show that the power-law exponent in the Ra - Nu relationship is about 0.2 (Roberts 1979; Mitrovica & Jarvis 1987). Our high-viscosity lid models produce similar results, with b in the range 0.17 to 0.20. For a given lower mantle viscosity, viscosity model 3 has a smaller vertically averaged viscosity than the other two viscosity models. Consequently, at a given Ra , viscosity model 3 has a higher Nu than the other two viscosity models (Fig. 12c).

The heat flow anomaly results for the three models with high-viscosity lids show vastly different slopes as a function of Ra . The three viscosity models give virtually the same heat flow at $Ra = 10^6$. If projected to higher Ra , viscosity model 1 would predict a larger peak heat flow than the other models. Given that the overall heat flow is highest for viscosity model 3, it is surprising that viscosity model 1 could ever have a higher peak heat flow than viscosity model 3. Our models use an imposed high-viscosity lid of fixed thickness, whereas in the temperature-dependent viscosity case, the high-viscosity layer would be thinner near the plume axis than elsewhere. This should lead to an increased heat flow anomaly near the plume axis in the temperature-dependent viscosity case. The flat slope of the heat flow- Ra relationship for viscosity model 3 may be related to our use of the same fixed lid thickness at varying Ra . If this explanation is correct, then the curves for viscosity models 1 and 2 are also likely to flatten out with further increases in Ra . Although the results shown in Fig. 12(d) for $Ra = 10^6$ are consistent with at least some observations of hotspot heat flow anomalies (e.g., Von Herzen *et al.* 1982; Detrick *et al.* 1986), because of the difficulties outlined above, we do not attempt a detailed comparison between our heat flow results and observations.

EFFECTS OF VARIATION IN ASPECT RATIO

Until now, we have assumed an aspect ratio of 1, consistent with the experimental results of Nataf & Richter (1982). On the other hand, Christensen & Yuen (1988) numerically studied a 2-D Cartesian box of aspect ratio 12. The individual convection cells that developed within the larger box typically had an aspect ratio of about 1.5, with some variation about the mean. Judging from the spacing between hotspots, an average aspect ratio for terrestrial mantle plumes is about 0.5, although there is likely to be some variation about this value. For example, relatively isolated and vigorous plumes such as Hawaii may have 'feeding zones' in the lower thermal boundary layer that are larger than normal, implying aspect ratios that are also larger than average. Assuming whole mantle convection, our aspect ratio 1 models predict swell widths that are consistent with the observed widths of Beta Regio and other highland regions on Venus (Kiefer & Hager 1991). It is not clear what causes plume swells to be nearly twice as broad on Venus as they are on Earth. In this section, we examine how varying the aspect ratio over the range 0.5 to 1.4 affects a plume's structure.

Figure 13 illustrates how varying the aspect ratio affects the thermal structure of a plume. Fig. 13(a) shows a cylindrical model with a high-viscosity lid (viscosity model 1), $Ra = 10^5$, and an aspect ratio of 1.4. In comparison with

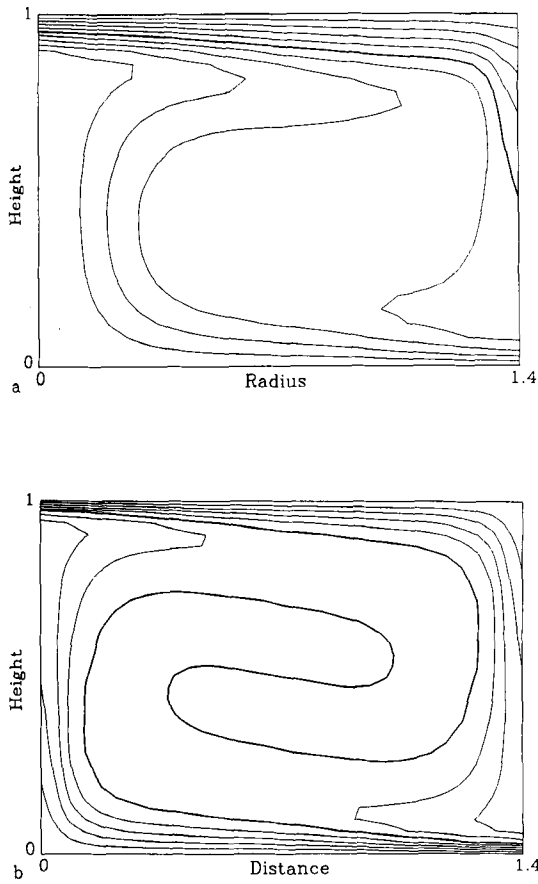


Figure 13. Isotherms for bottom heated convection at $Ra = 10^5$ and aspect ratio 1.4. The contour interval is 0.1. (a) Cylindrical geometry (model 34). (b) Cartesian geometry.

a similar model of aspect ratio 1.0 (Fig. 3), the upwelling plume in Fig. 13(a) is significantly broadened. This broadening is necessary to transport the additional heat introduced at the base of the cylinder when the aspect ratio is increased. A similar broadening is also observed with increasing aspect ratio for isoviscous cylindrical models. Fig. 13(b) shows an isoviscous Cartesian model with $Ra = 10^5$ and aspect ratio 1.4. Figs 4(a) and 13(b) show that very little broadening of the upwellings and downwellings occurs in the large aspect ratio Cartesian case. In cylindrical geometry, the basal area and the amount of heat a plume must transport increases as the square of the aspect ratio, whereas in Cartesian geometry, the basal area is only a linear function of the aspect ratio. This difference qualitatively accounts for the greater plume broadening in the cylindrical case.

Figure 14 shows how varying the aspect ratio affects the geoid anomaly, topographic uplift, and Nusselt number for cylindrical geometry plumes. The models shown in Fig. 14 have $Ra = 10^5$, use viscosity model 1, and vary the aspect ratio. The geoid anomaly and topographic uplifts refer to the peak values on the axis of the cylinder, while the Nusselt number is a volume-average. As shown in Figs 14(a) and (b), both the geoid and the topography are approximately linear functions of the aspect ratio. The solid lines are least-squares best fits and the triangles are model results.

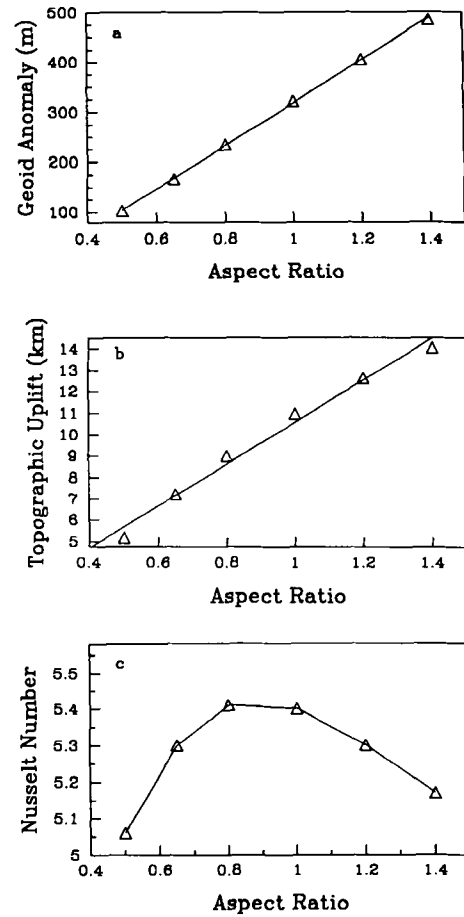


Figure 14. Effects of varying aspect ratio. Triangles are results for models 13 and 30–34. The lines in panels (a) and (b) are least-squares best fit straight lines to the model results, as discussed in the text. (a) Geoid anomaly at plume centre. (b) Topographic uplift at plume centre. (c) Volume-averaged Nusselt number.

These fits can be expressed as

$$\frac{\delta N}{\delta N_1} = 1.3 A - 0.3 \quad (15a)$$

and

$$\frac{\delta h}{\delta h_1} = 0.89 A + 0.07. \quad (15b)$$

In equation (15a), δN is the geoid anomaly, δN_1 is the geoid anomaly at aspect ratio 1.0, and A is the aspect ratio. Similarly, in equation (15b), δh is the topographic uplift and δh_1 is the topographic uplift at aspect ratio 1.0. There is some concave downward curvature in the results shown in Fig. 14(b), although the linear correlation is good ($r^2 = 0.99$). The broadening of the plume with increasing aspect ratio implies an increased amount of long-wavelength loading. Because long wavelengths couple more efficiently to the surface than short wavelengths, this implies an increasing topographic uplift with increasing aspect ratio. The increased mass anomalies due to the higher topography leads to a larger geoid. On Mars, the Tharsis and Elysium swells have different horizontal scales, suggesting that their

underlying convective upwellings have different aspect ratios. An effect similar to that shown in Figs 14(a) and (b) may contribute to the different geoid anomalies and topographic elevations in these regions (Kiefer & Hager 1989).

Figure 14(c) shows that Nu has a maximum value between aspect ratios 0.8 and 1.0. The total variation in Nu is less than 7 per cent over the range of aspect ratios studied. In Cartesian geometry, both Hansen & Ebel (1984) and Olson (1987) found Nu maxima at aspect ratios slightly less than 1.0.

TIME-DEPENDENT CONVECTION

Our finite element calculations use an implicit time-stepping routine, which allows us to use time-steps that are significantly larger than allowed by the Courant condition in explicit time-stepping routines. As a result, we can obtain steady-state solutions efficiently whenever such solutions exist. We have found steady solutions for all of the models listed in Table 2, where steady-state is defined as no change in either the heat flux or kinetic energy of the flow at the level of 1 part in 10^5 for 100 or more time steps. However, use of large time-steps with an implicit technique may produce an apparently steady solution that would actually be time-dependent if calculated using the Courant condition time-step. We have therefore examined several of our models using the Courant time-step and running the calculation for several over-turn times to determine if the solutions are truly steady-state.

Several parameters are believed to affect the development of time-dependent convection. Jarvis (1984) suggested that high Rayleigh numbers favour time-dependent convection. Ceuleneer *et al.* (1988) found that pronounced contrasts between upper and lower mantle viscosities also favours the development of time-dependence. Based on these considerations, we tested Model 29 for possible time-dependence. This model uses $Ra = 10^6$ and viscosity model 3 (asthenosphere viscosity = $0.01 \times$ lower mantle viscosity). When calculated on a 65×65 grid using a Courant time-step, this model is weakly time-dependent. Specifically, we observe the formation of instabilities in the upper thermal boundary layer that detach from the top boundary and descend along the outer side wall as discrete blobs. The upwelling plume, in contrast, appears to be steady. Over the course of several over-turn times, we observed variations in the peak geoid and peak topographic uplift of 3 to 4 per cent and variations of 2 per cent in the volume-averaged Nusselt number. Because of the relatively weak time-dependence observed for this model, we have not tested our other $Ra = 10^6$ models for time-dependence. At higher values of Ra , however, it seems possible that all three of our standard viscosity models will become time-dependent. Inclusion of temperature-dependent rheology might also enhance the development of time-dependent flow.

Several recent studies have shown that large aspect ratios can lead to time-dependent convective flow (Christensen 1987; Hansen & Ebel 1988; Weinstein, Olson & Yuen 1989). We tested our model 34 for possible time-dependence. This model was calculated on a 33×33 grid. It has $Ra = 10^5$ and an aspect ratio of 1.4 and uses viscosity model 1. When calculated for 1000 Courant time-steps, we

find no evidence for time-dependent behaviour in this model.

CONCLUSIONS

Observations of geoid anomalies, topographic uplift, and the distribution of volcanism suggest that at least some terrestrial hotspots, including several of the most prominent ones, and some highland features on Venus are due to convective upwellings that extend from deep in the mantle to the surface and have an approximately cylindrical geometry. We have modelled mantle plumes using cylindrical, axisymmetric geometry and depth-dependent viscosity. Our models do not include the effects of spherical geometry or temperature-dependent viscosity, although both effects deserve consideration in future studies. Most previous numerical models of mantle plumes have used a sheet-like, 2-D Cartesian upwelling. We find, however, that sheet-like and cylindrical upwellings produce significantly different geoid and topography signatures. The geoid anomaly and topography uplift are relatively insensitive to the details of the rheology of thermal lithosphere, provided that the surface layer has a viscosity that is at least 1000 times the interior viscosity. Increasing the Rayleigh number or including a low-viscosity asthenosphere decreases the geoid anomaly and topographic uplift associated with plumes, while increasing the aspect ratio increases both the geoid and topography. Detailed applications of our model results to observations of highland swells on Venus are presented by Kiefer & Hager (1991).

ACKNOWLEDGMENTS

We thank Arthur Raefsky for providing the finite element code used in this study. Mike Gurnis, Louise Kellogg, and Scott King provided helpful comments at various stages of this work, and Andy Ingersoll and Dave Stevenson provided reviews of an earlier draft of this manuscript. This research was supported by NASA Grant NAGW-1445. California Institute of Technology Division of Geological and Planetary Sciences Contribution Number 4864.

REFERENCES

- Anderson, D. L., 1987. A seismic equation of state: II. Shear properties and thermodynamics of the lower mantle, *Phys. Earth planet. Inter.*, **45**, 307–323.
- Basaltic Volcanism Study Project, 1981. *Basaltic Volcanism on the Terrestrial Planets*, Pergamon Press, Elmsford, NY.
- Baumgardner, J. R., 1988. Application of Supercomputers to 3-D Mantle Convection, in *The Physics of the Planets*, pp. 199–231, ed. Runcorn, S. K., Wiley, New York.
- Bercovici, D., Schubert, G. & Zebib, A., 1988. Geoid and topography for infinite Prandtl number convection in a spherical shell, *J. geophys. Res.*, **93**, 6430–6436.
- Bercovici, D., Schubert, G. & Glatzmaier, G. A., 1989a. Influence of heating mode on three-dimensional mantle convection, *Geophys. Res. Lett.*, **16**, 617–620.
- Bercovici, D., Schubert, G. & Glatzmaier, G. A., 1989b. Three-dimensional spherical models of convection in the Earth's mantle, *Science*, **244**, 950–955.
- Bills, B. G., Kiefer, W. S. & Jones, R. L., 1987. Venus gravity: A harmonic analysis, *J. geophys. Res.*, **92**, 10 335–10 351.

- Blankenbach, B. *et al.*, 1989. A benchmark comparison for mantle convection codes, *Geophys. J. Int.*, **98**, 23–38.
- Bonatti, E., Harrison, C. G. A., Fisher, D. E., Honnorez, J., Schilling, J.-G., Stipp, J. J. & Zentilli, M., 1977. Easter Volcanic Chain (Southeast Pacific): A mantle hot line, *J. geophys. Res.*, **82**, 2457–2478.
- Brooks, A. N. & Hughes, T. J. R., 1982. Streamline upwind/Petrov–Galerkin formulations for convection dominated flows with particular emphasis on the incompressible Navier–Stokes equations, *Comp. Meth. appl. Mech. Eng.*, **32**, 199–259.
- Ceuleneer, G., Rabinowicz, M., Monnereau, M., Cazenave, A. & Rosemberg, C., 1988. Viscosity and thickness of the sub-lithospheric low-viscosity zone: constraints from geoid and depth over oceanic swells, *Earth planet. Sci. Lett.*, **89**, 84–102.
- Christensen, U., 1984. Instability of a hot boundary layer and initiation of thermo-chemical plumes, *Annales Geophysicae*, **2**, 311–320.
- Christensen, U. R., 1987. Time-dependent convection in elongated Rayleigh–Benard cells, *Geophys. Res. Lett.*, **14**, 220–223.
- Christensen, U. & Yuen, D., 1988. On the aspect ratio of Rayleigh–Benard convection cells, *Geophys. Res. Lett.*, **15**, 597–600.
- Clague, D. A. & Dalrymple, G. B., 1987. The Hawaiian–Emperor Volcanic Chain: geologic evolution, *US Geological Survey Professional Paper 1350*, 5–54.
- Courtney, R. C. & White, R. S., 1986. Anomalous heat flow and geoid across the Cape Verde rise: evidence for dynamic support from a thermal plume in the mantle, *Geophys. J. R. astr. Soc.*, **87**, 815–867.
- Crough, S. T., 1978. Thermal origin of mid-plate hotspot swells, *Geophys. J. R. astr. Soc.*, **55**, 451–469.
- Crough, S. T., 1982. Geoid height anomalies over the Cape Verde Rise, *Mar. geophys. Res.*, **5**, 263–271.
- Crough, S. T., 1983. Hotspot swells, *Ann. Rev. Earth planet. Sci.*, **11**, 165–193.
- Crough, S. T. & Jurdy, D. M., 1980. Subducted lithosphere, hotspots, and the geoid, *Earth planet. Sci. Lett.*, **48**, 15–22.
- Daly, S. F. & Raefsky, A., 1985. On the penetration of a hot diapir through a strongly temperature-dependent viscosity medium, *Geophys. J. R. astr. Soc.*, **83**, 657–681.
- Davies, G. F., 1986. Mantle convection under simulated plates: effects of heating modes and ridge and trench migration, and implications for the core–mantle boundary, bathymetry, and the geoid and Benioff zones, *Geophys. J. R. astr. Soc.*, **84**, 153–183.
- Detrick, R. S. & Crough, S. T., 1978. Island subsidence, hotspots, and lithospheric thinning, *J. geophys. Res.*, **83**, 1236–1244.
- Detrick, R. S., Von Herzen, R. P., Parsons, B., Sandwell, D. & Dougherty, M., 1986. Heat flow observations on the Bermuda Rise and thermal models of midplate swells, *J. geophys. Res.*, **91**, 3701–3723.
- Duncan, R. A. & Clague, D. A., 1983. Pacific plate motion recorded by linear volcanic chains, in *The Ocean Basins and Margins*, Vol. 7A, *The Pacific Ocean*, pp. 89–121, eds Nairn, A. E. M., Stehli, F. G. & Uyeda, S., Plenum Press.
- Glatzmaier, G. A., 1988. Numerical simulations of mantle convection: time-dependent, three-dimensional, compressible, spherical shell, *Geophys. Astrophys. Fluid Dyn.*, **43**, 223–264.
- Hager, B. H., 1991. Mantle viscosity: a comparison of models from postglacial rebound and from the geoid, plate driving forces, and advected heat flux, in *Glacial Isostasy, Sea-level and Mantle Rheology*, pp. 493–513, eds Sabadini, R. & Lambeck, K., Kluwer Academic Publishers, Dordrecht.
- Hager, B. H. & Clayton, R. W., 1989. Constraints on the structure of mantle convection using seismic observations, flow models, and the geoid, in *Mantle Convection: Plate Tectonics and Global Dynamics*, pp. 657–763, ed. Peltier, W. R., Wiley, New York.
- Hager, B. H. & Richards, M. A., 1989. Long-wavelength variations in Earth's geoid: physical models and dynamical implications, *Phil. Trans. R. Soc. Lond.*, **A**, **328**, 309–327.
- Hansen, U. & Ebel, A., 1984. Experiments with a numerical model related to mantle convection: boundary layer behavior and small- and large-scale flows, *Phys. Earth planet. Inter.*, **36**, 374–390.
- Hansen, U. & Ebel, A., 1988. Time-dependent thermal convection—a possible explanation for a multi-scale flow in the earth's mantle, *Geophys. J.*, **94**, 181–191.
- Hofmann, A. W. & White, W. M., 1982. Mantle plumes from ancient oceanic crust, *Earth planet. Sci. Lett.*, **57**, 421–436.
- Ho-Liu, P., Hager, B. H. & Raefsky, A., 1987. An improved method of Nusselt number calculation, *Geophys. J. R. astr. Soc.*, **88**, 205–215.
- Houseman, G., 1988. The dependence of convection planform on mode of heating, *Nature*, **332**, 346–349.
- Houseman, G. A., 1990. The thermal structure of mantle plumes: axisymmetric or triple-junction?, *Geophys. J. Int.*, **102**, 15–24.
- Hughes, T. J. R., 1987. *The Finite Element Method*, Prentice-Hall, Englewood Cliffs, NJ.
- Jarvis, G. T., 1984. Time-dependent convection in the Earth's mantle, *Phys. Earth planet. Inter.*, **36**, 305–327.
- Jeanloz, R., & Richter, F. M., 1979. Convection, composition, and the thermal state of the lower mantle, *J. geophys. Res.*, **84**, 5497–5504.
- Jones, C. A., Moore, D. R. & Weiss, N. O., 1976. Axisymmetric convection in a cylinder, *J. Fluid Mech.*, **73**, 353–388.
- Kaneoka, I., Takaoka, N. & Upton, B. G. J., 1986. Noble gas systematics in basalts and a dunite nodule from Reunion and Grand Comore Islands, Indian Ocean, *Chem. Geol.*, **59**, 35–42.
- Kaula, W. M. & Phillips, R. J., 1981. Quantitative tests for plate tectonics on Venus, *Geophys. Res. Lett.*, **8**, 1187–1190.
- Kellogg, L. H. & Wasserburg, G. J., 1990. The role of plumes in mantle helium fluxes, *Earth planet. Sci. Lett.*, **99**, 276–289.
- Kiefer, W. S., 1990. Models for the formation of highland regions on Venus, *PhD thesis*, California Institute of Technology.
- Kiefer, W. S. & Hager, B. H., 1989. The role of mantle convection in the origin of the Tharsis and Elysium provinces of Mars (abstract), *MEVTV-LPI Workshop: Early Tectonic and Volcanic Evolution of Mars*, LPI Technical Report 89–04, pp. 48–50.
- Kiefer, W. S. & Hager, B. H., 1991. A mantle plume model for the equatorial highlands of Venus, *J. geophys. Res.*, in press.
- Kiefer, W. S., Richards, M. A., Hager, B. H. & Bills, B. G., 1986. A dynamic model of Venus's gravity field, *Geophys. Res. Lett.*, **13**, 14–17.
- Kurz, M. D., Meyer, P. S. & Sigurdsson, H., 1985. Helium isotopic systematics within the neo-volcanic zones of Iceland, *Earth planet. Sci. Lett.*, **74**, 291–305.
- Kurz, M. D., Jenkins, W. J., Schilling, J. G. & Hart, S. R., 1982. Helium isotopic variations in the mantle beneath the central North Atlantic Ocean, *Earth planet. Sci. Lett.*, **58**, 1–14.
- Kurz, M. D., Jenkins, W. J., Hart, S. R. & Clague, D., 1983. Helium isotopic variations in volcanic rocks from Loihi Seamount and the Island of Hawaii, *Earth planet. Sci. Lett.*, **66**, 388–406.
- McKenzie, D. & Bickle, M. J., 1988. The volume and composition of melt generated by extension of the lithosphere, *J. Petrol.*, **29**, 625–679.
- McKenzie, D. P., Roberts, J. M. & Weiss, N. O., 1974. Convection in the Earth's mantle: towards a numerical simulation, *J. Fluid Mech.*, **62**, 465–538.
- McKenzie, D., Watts, A., Parsons, B. & Roufousse, M., 1980. Planform of mantle convection beneath the Pacific Ocean, *Nature*, **288**, 442–446.

- McNutt, M., 1988. Thermal and mechanical properties of the Cape Verde Rise, *J. geophys. Res.*, **93**, 2784–2794.
- McNutt, M. & Shure, L., 1986. Estimating the compensation depth of the Hawaiian swell with linear filters, *J. geophys. Res.*, **91**, 13 915–13 923.
- Mitrovica, J. X. & Jarvis, G. T., 1987. A numerical study of thermal convection between rigid horizontal boundaries, *Geophys. Astrophys. Fluid Dyn.*, **38**, 193–224.
- Morgan, W. J., 1965. Gravity anomalies and convection currents: 1. A sphere and cylinder sinking beneath the surface of a viscous fluid, *J. geophys. Res.*, **70**, 6175–6187.
- Morgan, W. J., 1972a. Deep mantle convection plumes and plate motions, *Am. Assoc. Petrol. Geol. Bull.*, **56**, 203–213.
- Morgan, W. J., 1972b. Plate motions and deep mantle convection, *Geol. Soc. Am. Memoir* 132, 7–22.
- Nakada, M. & Lambeck, K., 1989. Late Pleistocene and Holocene sea-level change in the Australian region and mantle rheology, *Geophys. J.*, **96**, 497–517.
- Nataf, H. C. & Richter, F. M., 1982. Convection experiments in fluids with highly temperature-dependent viscosity and the thermal evolution of the planets, *Phys. Earth planet. Inter.*, **29**, 320–329.
- Okal, E. A. & Batiza, R., 1987. Hotspots: the first 25 years, in *Seamounts, Islands, and Atolls*, *Geophysical Monograph* 43, pp. 1–11, ed. Keating, B. H., Fryer, P., Batiza, R. & Boehlert, G. W., American Geophysical Union, Washington, DC.
- Olson, P., 1987. A comparison of heat transfer laws for mantle convection at very high Rayleigh numbers, *Phys. Earth planet. Inter.*, **48**, 153–160.
- Olson, P., Schubert, G. & Anderson, C., 1987. Plume formation in the D" layer and the roughness of the core–mantle boundary, *Nature*, **327**, 409–413.
- Parmentier, E. M., Turcotte, D. L. & Torrance, K. E., 1975. Numerical experiments on the structure of mantle plumes, *J. geophys. Res.*, **80**, 4417–4424.
- Parsons, B. & Daly, S., 1983. The relationship between surface topography, gravity anomalies, and temperature structure of convection, *J. geophys. Res.*, **88**, 1129–1144.
- Pekeris, C. L., 1935. Thermal convection in the interior of the Earth, *Mon. Not. R. astr. Soc., Geophys. Suppl.*, **3**, 343–367.
- Ricard, Y., Fleitout, L. & Froidevaux, C., 1984. Geoid heights and lithospheric stresses for a dynamic earth, *Annales Geophysicae*, **2**, 267–286.
- Richards, M. A. & Hager, B. H., 1984. Geoid anomalies in a dynamic earth, *J. geophys. Res.*, **89**, 5987–6002.
- Richards, M. A., Hager, B. H. & Sleep, N. H., 1988. Dynamically supported geoid highs over hotspots: observations and theory, *J. geophys. Res.*, **93**, 7690–7708.
- Roberts, G. O., 1979. Fast viscous Benard convection, *Geophys. Astrophys. Fluid Dyn.*, **12**, 235–272.
- Robinson, E. M., Parsons, B. & Daly, S. F., 1987. The effect of a shallow low viscosity zone on the apparent compensation of mid-plate swells, *Earth planet. Sci. Lett.*, **82**, 335–348.
- Robinson, E. M. & Parsons, B., 1988. Effects of a shallow low-viscosity zone on the formation of midplate swells, *J. geophys. Res.*, **93**, 3144–3156.
- Sandwell, D. T. & Poehls, K. A., 1980. A compensation mechanism for the central Pacific, *J. geophys. Res.*, **85**, 3751–3758.
- Schubert, G., Bercovici, D. & Glatzmaier, G. A., 1990. Mantle dynamics in Mars and Venus: influence of an immobile lithosphere on three-dimensional mantle convection, *J. geophys. Res.*, **95**, 14 105–14 129.
- Sleep, N. H., 1984. Tapping of magmas from ubiquitous mantle heterogeneities: an alternative to mantle plumes?, *J. geophys. Res.*, **89**, 10 029–10 041.
- Sleep, N. H., 1990. Hotspots and mantle plumes: some phenomenology, *J. geophys. Res.*, **95**, 6715–6736.
- Stevenson, D. J., Spohn, T. & Schubert, G., 1983. Magnetism and thermal evolution of the terrestrial planets, *Icarus*, **54**, 466–489.
- Travis, B., Weinstein, S. & Olson, P., 1990. Three-dimensional convection planforms with internal heat generation, *Geophys. Res. Lett.*, **17**, 243–246.
- Tryggvason, K., Husebye, E. S. & Stefansson, R., 1983. Seismic image of the hypothesized Iceland hotspot, *Tectonophysics*, **100**, 97–118.
- Turcotte, D. L. & Oxburgh, E. R., 1978. Intra-plate volcanism, *Phil. Trans. R. Soc. Lond.*, **A**, **288**, 561–579.
- US Geological Survey, 1984. Topographic and shaded relief maps of Venus, *Miscellaneous Investigations Series Map I-1562*, Boulder, CO.
- Von Herzen, R. P., Detrick, R. S., Crough, S. T., Epp, D. & Fehn, U., 1982. Thermal origin of the Hawaiian swell: heat flow evidence and thermal models, *J. geophys. Res.*, **87**, 6711–6723.
- Watts, A. B., McKenzie, D. P., Parsons, B. E. & Roufousse, M., 1985. The relationship between gravity and bathymetry in the Pacific Ocean, *Geophys. J. R. astr. Soc.*, **83**, 263–298.
- Weinstein, S. A., Olson, P. L. & Yuen, D. A., 1989. Time-dependent large aspect-ratio thermal convection in the Earth's mantle, *Geophys. Astrophys. Fluid Dyn.*, **47**, 157–197.
- Wilson, J. T., 1963. A possible origin of the Hawaiian Islands, *Can. J. Phys.*, **41**, 863–870.
- Wyllie, P. J., 1988. Solidus curves, mantle plumes, and magma generation beneath Hawaii, *J. geophys. Res.*, **93**, 4171–4181.
- Yuen, D. A. & Peltier, W. R., 1980. Mantle plumes and the thermal stability of the D" layer, *Geophys. Res. Lett.*, **7**, 625–628.
- Zhang, Y. S. & Tanimoto, T., 1989. Three-dimensional modelling of upper mantle structure under the Pacific Ocean and surrounding area, *Geophys. J. Int.*, **98**, 255–269.